

Precision half-life determination for the β^+ emitter ^{13}N

J. Long,¹ C. R. Nicoloff^{1,2,3}, D. W. Bardayan,¹ F. D. Becchetti,⁴ D. Blankstein,¹ C. Boomershine¹, D. P. Burdette,¹ M. A. Caprio¹, L. Caves,¹ P. J. Fasano¹, B. Frentz¹, S. L. Henderson,¹ J. M. Kelly,¹ J. J. Kolata¹, B. Liu,¹ P. D. O'Malley,¹ S. Y. Strauss,¹ R. Zite,¹ and M. Brodeur^{1,*}

¹Department of Physics and Astronomy, University of Notre Dame, Notre Dame, Indiana 46556, USA

²Physics Department, Michigan State University, East Lansing, Michigan 48824, USA

³National Superconducting Cyclotron Laboratory, East Lansing, Michigan 48824, USA

⁴Physics Department, University of Michigan, Ann Arbor, Michigan 48109, USA

 (Received 4 June 2021; revised 12 August 2022; accepted 30 August 2022; published 19 October 2022)

A new precision half-life measurement of ^{13}N has been conducted using the *TwinSol* β -counting station at the University of Notre Dame. The measured value of $t_{1/2}^{\text{new}} = 597.05(19)$ s differs from the previous world value by about 2.8σ . An evaluation of the ^{13}N half-life results in a $t_{1/2}^{\text{world}} = 597.19(22)$ s. Updated standard model predictions for the Fermi to Gamow-Teller mixing ratio ρ and its associated correlation parameters have been calculated using the new ^{13}N world half-life in preparation for a future measurement of the mixing ratio. Finally, an *ab initio* no-core configuration interaction (NCCI) calculation for the $B(\text{GT})$ of this decay, carried out using the Daejeon16 interaction, has been performed, revealing the need for higher-order chiral corrections.

DOI: [10.1103/PhysRevC.106.045501](https://doi.org/10.1103/PhysRevC.106.045501)

I. INTRODUCTION

Allowed β -decay transitions in light nuclei are the subject of many efforts in searching for standard model-violating scalar and tensor currents [1,2]. Furthermore, it is superallowed $0^+ \rightarrow 0^+$ β -decay transitions that impose the strongest constraint on a possible violation of the conserved vector current (CVC) hypothesis due to the presence of a standard model-violating scalar current [3]. Such constraint was made possible by the precise measurements of the half-lives, the branching ratios, and the masses entering into the ft -value calculations of the lightest isotopes, ^{10}C and ^{14}O [3]. Superallowed mixed β -decay transitions between light mirror nuclei have also generated renewed interest with the precision mass [4] and half-life [5] measurements of ^{11}C . Superallowed mixed β -decay transitions are not only one more avenue to obtain the V_{ud} matrix element [6] and test the CVC hypothesis, but they can also probe for the existence of right-handed neutrinos [2]. These transitions can also be used to test the prediction of various calculation methods of the isospin symmetry-breaking correction, which is essential for the extraction of V_{ud} . In particular, light nuclei such as ^{13}N can be approached via multiple *ab initio* calculation methods, making it an ideal test case for obtaining more accurate isospin symmetry-breaking corrections [7]. All of these, however, require an experimental determination of the Fermi-to-Gamow Teller mixing ratio ρ , which is only known precisely for five transitions [6].

Therefore, in preparation for a future determination of ρ that would allow the above studies in ^{13}N , the experimental

quantities entering into the computation of its ft value need to be established. To that end, we have measured, for the first time in over 40 years, the half-life of ^{13}N using the β -counting station at the University of Notre Dame's Nuclear Science Laboratory (UND NSL) *TwinSol* radioactive ion-beam facility. We also present the first steps towards an *ab initio* determination of the ^{13}N isospin symmetry-breaking correction.

II. EXPERIMENTAL METHOD

Similar to previous precision half-life measurements conducted at the NSL, a radioactive ion beam (RIB) of ^{13}N was produced utilizing the *TwinSol* twin-solenoid facility [8]. First, a cesium sputtering ion source with a graphite cathode was used to produce an intense stable ^{12}C primary beam that was then accelerated using a 10 MV tandem accelerator set to a terminal voltage of 6.8 MV. Following the accelerator, the stable beam passes through a mass-analyzing bending magnet, which separates charge states and selects only $^{12}\text{C}^{4+}$ at 34 MeV, which is then sent to *TwinSol* for RIB production.

The stable ^{12}C beam collides with a deuterium gas target located directly in front of *TwinSol* to create a mixed secondary beam. The beam then goes through the first *TwinSol* solenoid to separate the ^{13}N from the majority of other stable components of the beam, which is further focused by the second solenoid to create a RIB of ^{13}N . This radioactive beam is then sent to the NSL β -counting station [9,10].

There, the beam is implanted into a 0.25-mm-thick gold foil that is surrounded by a tantalum frame [11,12]. After implantation, the target, which is attached to an aluminum arm, is rotated 180 degrees from the implantation position to the counting position [10]. There, the sufficiently energetic

* mbrodeur@nd.edu

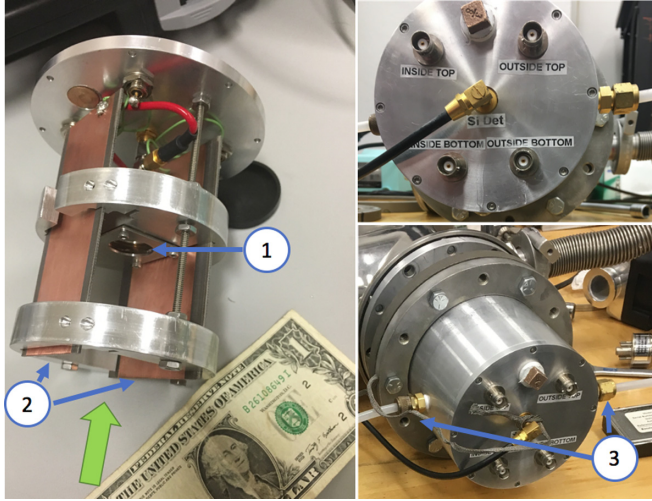


FIG. 1. Photographs of the newly constructed ACBAR particle identification gas cell interior frame (left), the back plate of the frame (top right), and the frame placed inside the chamber (bottom right). (1) The silicon detector, (2) the anode and cathode plates, and (3) P10 gas feed-through lines. The large green arrow indicates how the beam enters the gas cell.

β particles emitted as a result from the disintegration of ^{13}N first travel through a thin aluminum foil before impinging on a 1-mm-thick plastic scintillator, after which the produced photons are guided to a photomultiplier tube (PMT) via a cemented light guide wrapped in aluminum.

The electric pulses produced by the PMT then pass through a discriminator whose threshold is adjusted to minimize background pulses. Next the signal is replicated and sent to the event trigger, a custom-made module from the NSL based on an Oak Ridge National Laboratory design. The event trigger module generates a 100 Hz clock signal and also a busy signal. This busy signal acts as a veto and prevents the recording of data when data is already being processed. This step is critical in ensuring that our dead time is “nonextendable” [13]. The data are then saved in a list format where each event is a separate entry stamped with the real and live time value when the event occurred.

Finally, an electrostatic steerer is used to deflect the primary beam prior to the tandem during the counting phase to avoid the production of radioactive contaminants that would influence the half-life measurement.

A. ACBAR gas cell detector

Before starting the half-life measurements, the purity of the RIB at the β -counting station was assessed using the newly constructed Argon-methane cocktail beam assessment for RIB’s (ACBAR) small gas cell. A photograph of the ACBAR interior frame of the gas chamber is given in Fig. 1 and its dimensions are given in Table I. The gas cell has a 3- μm -thick mylar window and operates by relying on the P10 gas inside the detector being ionized when incident nuclei enter the cylindrical chamber.

TABLE I. Various dimensions for the ACBAR PID ionization chamber.

Dimension	Size (cm)
Length	12.0
Diameter	7.2
Plate separation	3.9

A homogeneous electric field is created using two electrodes parallel to the beam path. The electrons released via ionization of the gas are collected to determine the initial energy lost by the incoming particle. The final energy is then measured using a silicon surface-barrier detector placed at the back of the chamber. Plotting the energy lost in the gas vs the energy deposited in the silicon detector allows for beam characterization, as can be seen in Fig. 2.

The ACBAR design possesses a few advantages over the standard silicon detector telescope that makes it more versatile. Standard ΔE silicon detectors are typically 20 μm or thicker, which limits the minimum incoming beam energy and restricts the characterization of high- Z beams. Since P10 gas is used as ΔE , the ACBAR gas cell is able to measure the energy lost for heavier or lower-energy incoming particles without stopping them. The location of the silicon detector can also be adjusted along the axis of the chamber. In addition, the particle identification (PID) gas cell pressure can be raised or lowered, allowing for a wide range of particle identification.

Using this new gas cell, no significant radioactive contaminants, within the limits of the measurement uncertainty, were identified as can be seen in Fig. 2.

B. ^{13}N data collection

The ^{13}N half-life measurement was comprised of a series of 17 runs, each consisting of one implantation and one counting period. Fifteen of these runs had a counting period of 25 half-lives, or about 4.2 hours. The two remaining runs,

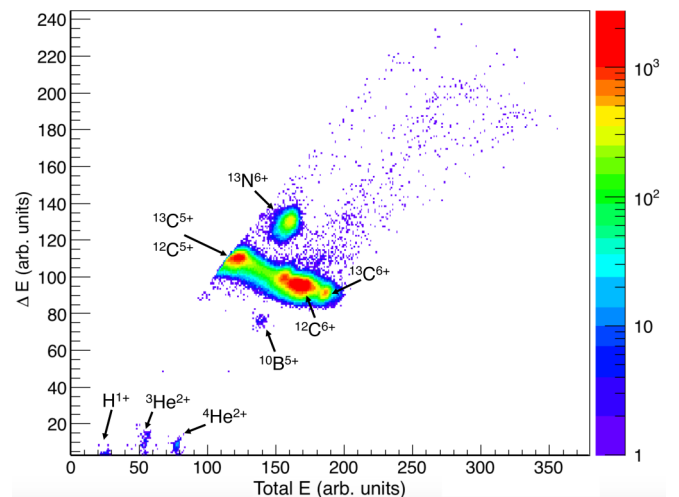


FIG. 2. Particle identification plot of the incoming cocktail beam separated by the *TwinSol* facility at the β -counting station.

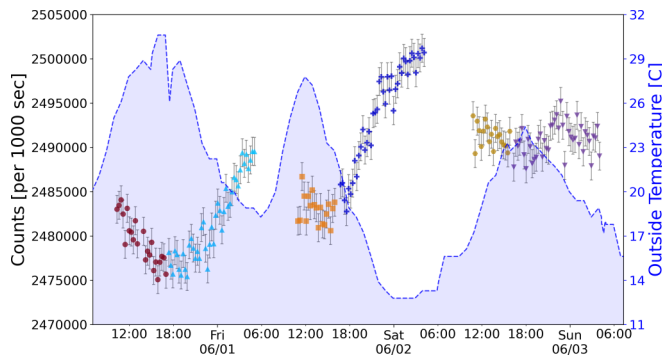


FIG. 3. A representative sample of offline PMT test run count rates (per 1000 s) superimposed over outdoor temperatures from a local airport.

of which one was taken before and one after the 15 standard runs, were implanted for the same amount of time but instead were counted over 50 half-lives, or about 8.3 hours, in order to probe for long-lived contamination. The beam was implanted for 1800 s for each run. For each run either the PMT bias or the PMT discriminator signal threshold were varied to probe for any possible systematic effects that would affect the measurement.

C. Study of the photomultiplier tube stability

Because the counting period for each run was on the order of hours, the stability of the PMT used to count the ^{13}N beta decays was critical for the accuracy of the resulting half-life. To probe the stability of the PMT over long durations, a β^- -emitting ^{90}Sr source [with 28.90(3) year half-life] was attached to the rotating paddle and placed facing the plastic scintillator. Several runs over the period of multiple days were taken.

While the count rate was observed to change by as much as 0.5% in a period of 6 hours, stable count rate was also observed. Figure 3 shows such a situation for a period of several days and indicate that the count rate measured by the PMT is sensitive to fluctuations in temperature. To illustrate this, outdoor temperatures from a nearby airport are superimposed over the count rate data acquisition in Fig. 3. Indoor temperatures during this time period were, unfortunately, not available. Figure 3 indicates that the count rate is affected by large fluctuations in outside temperature such as nighttime cool down. On the other hand, the count rate remains stable when the outside temperature stays in the 20–25 °C range. There is also a time delay of approximately 4–6 hours between outdoor changes and count rate variations. Figure 4 shows the indoor temperature in the laboratory (after it started to be recorded) together with the outdoor temperature for a similar time of the year as when the data in Fig. 3 were taken. Note again the time delay of approximately 4–6 hours between outdoor temperature changes and indoor temperature changes. Figure 4 shows that the indoor temperature remains stable if the outdoor temperature is stable around 20–25 °C, while being affected by a sharp drop in temperature, which is a similar behavior as seen in the count rate. Hence, to mitigate

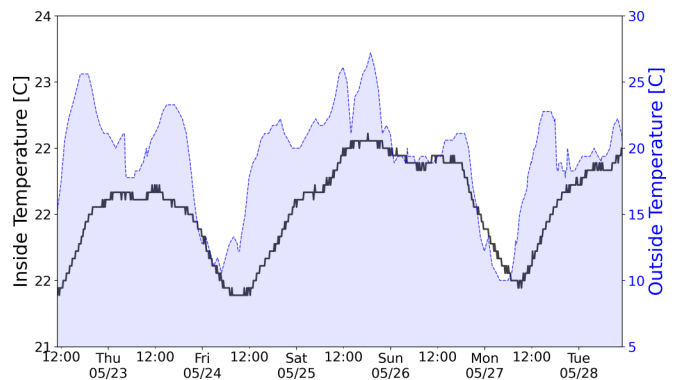


FIG. 4. A sample showing the relationship between outdoor and indoor temperatures. This temperature data were recorded approximately one year after the offline PMT stability test runs.

systematic changes in count rate due to temperature fluctuations, only runs where the indoor temperature changed within the 0.1 °C resolution of our sensor were kept. Figure 5 shows these kept runs. Runs 3, 4, and 8–10 were all rejected due to the observed temperature increase in the course of these measurements as indicated by the black line. Figure 5 also includes the outdoor temperature. Because the ^{13}N data were taken during the early spring, the count rate was most stable when the outside temperature did not fluctuate too much or it was sufficiently cold. In the end, 12 cycles were kept in the following analysis.

III. DATA ANALYSIS

Two methods have been used as part of the analysis: the run-by-run and sum fit [14]. The latter method was used to obtain the ^{13}N half-life and the former to investigate possible systematic effects. This procedure was also applied for other recent precision half-life measurements conducted at the NSL [5,10–12,15,16]. Additionally, the half-life analysis of ^{13}N was performed independently by two different members of the group to ensure the consistency of the results. For both the run-by-run and sum fit methods, the event-by-event data are first binned and a correction for the missed counts due to dead time is applied.

A. Determination of dead time per event

The dead time per event for this experiment has been extracted by using two different methods [11]. In the first method, the dead time is calculated by taking the difference between the unvetoes time given by our clock and the time vetoed when events are registered. This clock difference is then divided by the total number of counts to extract a dead time per event in a given run. The average is then taken over the 12 temperature-stable runs to obtain the dead-time per event for this method, which was found to be $\tau = 56.24(15) \mu\text{s}$.

The second determination used the source-pulsar method [17], which requires the use of a radioactive source and a pulse generator, as described in Ref. [11]. The dead time per event was measured immediately after the experiment

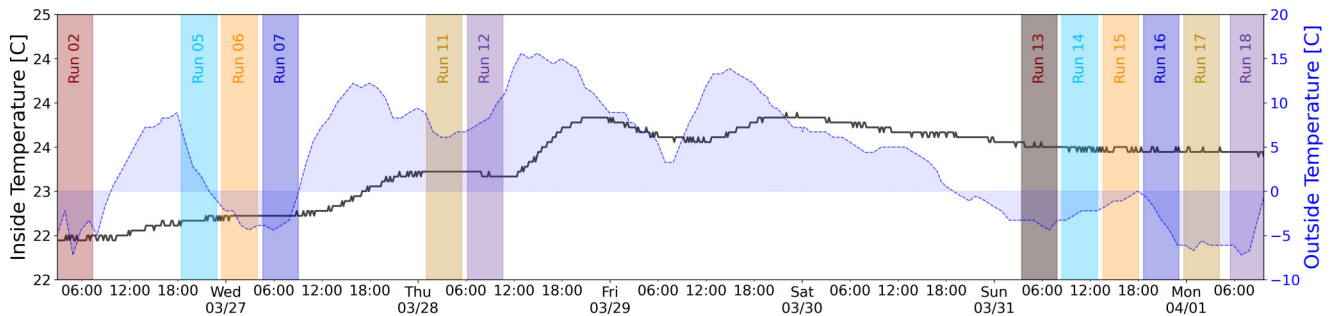


FIG. 5. Temperatures from inside the NSL and from a local airport were both recorded at the time of the ^{13}N experiment. The data acquisition runs during which the indoor temperature was stable to less than 0.1°C are shown as vertical bars representing time periods.

resulting in $\tau = 56.33(14) \mu\text{s}$. These measurements are consistent with one another. Taking the weighted average of these two dead time measurements results in the dead time per event of $\tau = 56.28(10) \mu\text{s}$ used in the half-life analysis.

B. Half-life determination

The ^{13}N data were fit by using the so-called summed fit method [14]. All of the runs were trimmed to the same length of approximately 25 ^{13}N half-lives such that all the data could be combined and fit together. Then the data were histogrammed into 500 bins and the number of counts in each bin and their variance was corrected for losses due to the dead time inherent in the detection system. After, the number of counts in a given bin for all 12 runs were summed.

Finally, the integral of the decay rate

$$r(t) = r_0 e^{-(\ln 2)t/t_1} + b, \quad (1)$$

where r_0 is the initial rate, t_1 is the half-life, and b is the background rate in each bin, was fit to the summed data. An iterative least-squares fitting method was used to approach the Poisson maximum-likelihood [10,14,18]. The results from that method were cross-checked with a second common approach that involved the minimization of a χ^2 derived from Poisson statistics [19,20]. Nearly identical results were obtained from both approaches [5,10].

The result and residuals of the summed fit procedure are shown in Fig. 6. Both of the above fit method yields a half-life of $597.05(14) \text{ s}$, with a reduced $\chi^2_\nu = 0.90$ and a mean residual value of 0.007 having a standard deviation of 0.95. Together these imply that the fitting procedure fits the data well and explains the observed features.

C. Uncertainty estimation

Several sources of uncertainty in the half-life fitting procedure were investigated. These sources include the effects from the uncertainty in the dead time value, the precision of the clock, the effect of the time-binning choice, and possible contaminations [5]. These results are described in detail below and summarized in Table II.

1. Dead time uncertainty

To probe the effect of the $0.10 \mu\text{s}$ uncertainty on the $56.28 \mu\text{s}$ dead time per event, the fitting procedure was re-

peated twice using the extreme values within the uncertainty, which are $\tau = 56.38 \mu\text{s}$ and $\tau = 56.18 \mu\text{s}$. Half the difference of the ^{13}N half-lives resulting from these two fits, 35 ms, is then added in quadrature to the overall ^{13}N half-life uncertainty.

2. Clock uncertainty

The clock frequency, nominally 100 Hz, was measured directly with a Teledyne LeCroy 500 MHz oscilloscope. This resulted in a measured clock value of $99.9996(10) \text{ Hz}$, which was used in the ^{13}N half-life analysis in Sec. III B. To determine the clock's systematic effect on the half-life, the fitting procedure was repeated with both the high and low values within the clock frequency uncertainty. The difference between these two results divided by two gives a systematic uncertainty of 6 ms. This value was then added in quadrature to the overall ^{13}N half-life uncertainty.

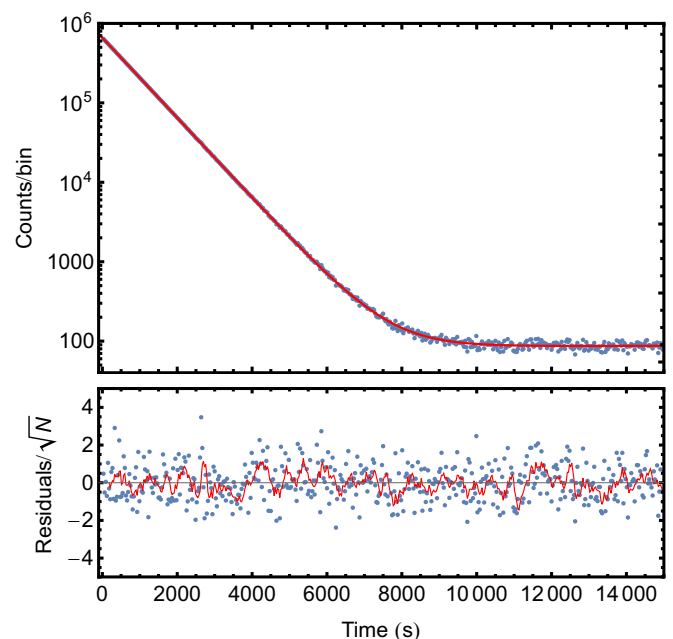


FIG. 6. Summed β -decay curve for all 12 runs. Below are the residuals of the fit divided by the square root of the number of ions in a given bin N with a red line over the residuals representing the five-point moving average.

TABLE II. Various sources contributing to the overall systematic uncertainty of the ^{13}N half-life.

Source	Uncertainty (ms)
Dead time	35
Contamination	41
Clock time	6
Binning	11
Total systematic uncertainty	55
Statistical uncertainty	144

3. Time-binning-choice uncertainty

To probe the effect of the time-binning choice the fitting procedure was repeated using a binning choice of 250 and 750 bins in addition to the original binning choice of 500 bins. The largest deviation between these three results came from comparing the results of 250 and 750 bins. This difference was equal to 11 ms and was added in quadrature to the overall ^{13}N half-life uncertainty.

4. Contamination-related considerations

The energy of the incoming ^{12}C was sufficiently low that it could not produce radioactive contaminants via a reaction with deuterium. Nevertheless, radioactive contaminants could have been produced by other reactions. Hence, the data were also probed for the influence of potentially unaccounted-for contaminants. To further probe for any unaccounted short-lived contaminants the leading bins of the total summed histogram were removed sequentially and a summed half-life fit performed on the remaining bins. Up to eight half-lives of the data were removed, corresponding to over 95% of all measured counts. If more points are removed after this, there are insufficient data left to perform a meaningful fit. The results of this procedure are shown at the top of Fig. 7, and no time-dependent systematic trends are apparent.

To probe for intermediate and longer-lived contaminants the fit function given in Eq. (1) was adjusted to account for the presence of a second radionuclide to take the form

$$r(t) = r_0(e^{-(\ln 2)t/t_1} + Re^{-(\ln 2)t/t_2}) + b, \quad (2)$$

where R is the contaminant to ^{13}N ratio, and t_2 is the contaminant half-life. We then fit Eq. (2) alternatively using the half-life of ^{11}C [1220.41(32) s] [5] and ^{15}O [122.27(6) s] [12] possible contaminants that could have been produced by reactions between the primary ^{12}C beam and trace amount of contaminant in the production cell, resulting in $R = 0.3(18) \times 10^{-4}$ and $0.2(11) \times 10^{-3}$, respectively. These ratios result in changes in the ^{13}N half-life of 32 and 19 ms, respectively.

To further probe the data for a potentially very-long-lived contamination, the fit function was modified a third time to include a linear background term of the form

$$r(t) = r_0e^{-(\ln 2)t/t_1} + Xt + b, \quad (3)$$

where X is a slope in the background produced from the decay of a very long-lived contaminant. If no very long-lived contaminant is present, an X result of zero is expected. The result

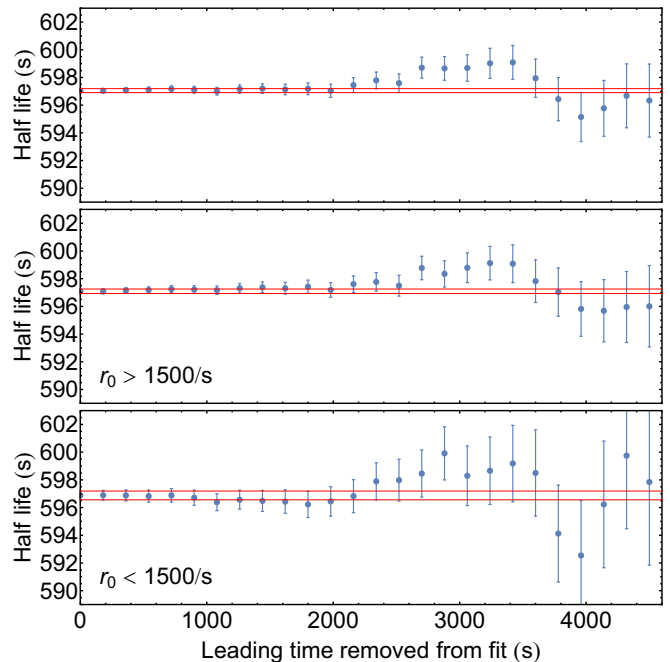


FIG. 7. Fitted half-lives for the total summed data with leading bins removed. The fit was then performed on the remaining bins for all the runs combined (top panel), runs with an initial counting rate above 1500 counts per second (center panel), and the single run with an initial counting rate below 1500 counts per second (bottom panel). Up to eight half-lives were removed for each case. The two red lines indicate the uncertainty on the *summed fit* without any bin removal.

for this fit is $X = 6.6(72) \times 10^{-7}$ and the resulting half-life differs from the one without a contaminant by 41 ms. Hence, to be conservative, the largest change of 41 ms was added as systematic uncertainty due to contamination.

5. Other systematic effects

To probe for other systematic effects, the data were fit on a run-by-run basis. The fit results for each run are shown in Fig. 8 as function of the initial activity and background. All cycles had an initial activity of less than 4 kHz. To investigate possible long-term and rate-dependent gain shifts of the PMT effect on the fitted half-life, we fit the data with increasingly more of the initial data removed. The results are shown in Fig. 7 for all cycles (top), for cycles with a counting rate above 1.5 kHz combined (middle) and cycles below 1.5 kHz (bottom). If the measurements were plagued by rate-dependent gain shifts, a greater lowering in the initial number of events (after dead time correction) should be observed for the high-rate cycle, which would affect the fitted half-life. Moreover, no significant long-term variations in the fitted half-life with leading time is observed. Therefore, this leads to the conclusion that the data are not affected by possible long-term and rate-dependent gain shifts at our level of sensitivity. The weighted average of these points give a result of 597.07(14) s, which agrees extremely well with the summed fit result.

Other systematic effects also explored include the influence of the PMT voltage and the PMT discriminator threshold

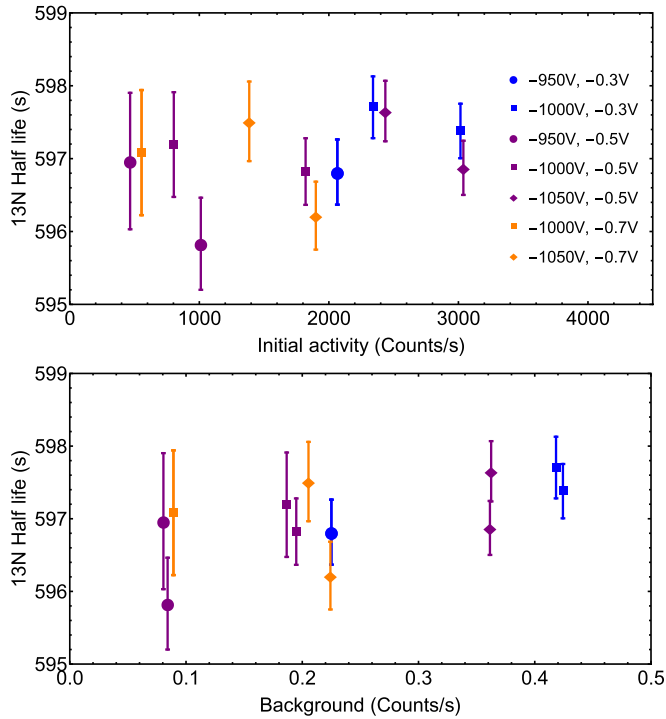


FIG. 8. Plot of half-lives of ^{13}N vs the initial activity (top panel) and the background activity (bottom panel) on a run-by-run basis. The point color corresponds to the PMT discriminator voltage and the point shape indicates the PMT voltage.

voltage. The PMT tube was set to -950 , -1000 , and -1050 volts and the PMT discriminator was set to -0.3 , -0.5 , and -0.7 volts. One of these parameters was changed for each of the 12 runs such that all possible combinations of both PMT and discriminator voltages leading to a meaningful activity were taken, as shown in Fig. 8. As can be seen in the figure, there are no apparent systematic effects due to these factors.

It should also be noted that, when the PMT discriminator threshold is changed from -0.3 to -0.7 V, more low-energy β s are being cut, which in turn reduces the background and observed activity. Similarly, lowering the PMT voltage will reduce the gain of the PMT, which result in lower amplitude pulses, some of which will be below the discriminator threshold and not be recorded. Hence, lowering either the PMT or discriminator threshold voltage results in a decrease of the observed activity and background rates as observed in Fig. 8. Since runs with lower activity will have fewer counts, a greater statistical spread in the resulting half-life will result, as studied in Ref. [5].

To further probe for any potential systematic effects due to the PMT voltage and the discriminator threshold voltage a summed fit was performed grouping the runs according to identical PMT voltage settings and identical discriminator threshold voltage settings. The results are summarized in Fig. 9. The weighted averages of the PMT voltage and the discriminator threshold groupings give the same result of $597.05(14)$ s, which is identical to the result obtained from the summed fit. The PMT voltage grouping Birge ratio [21]

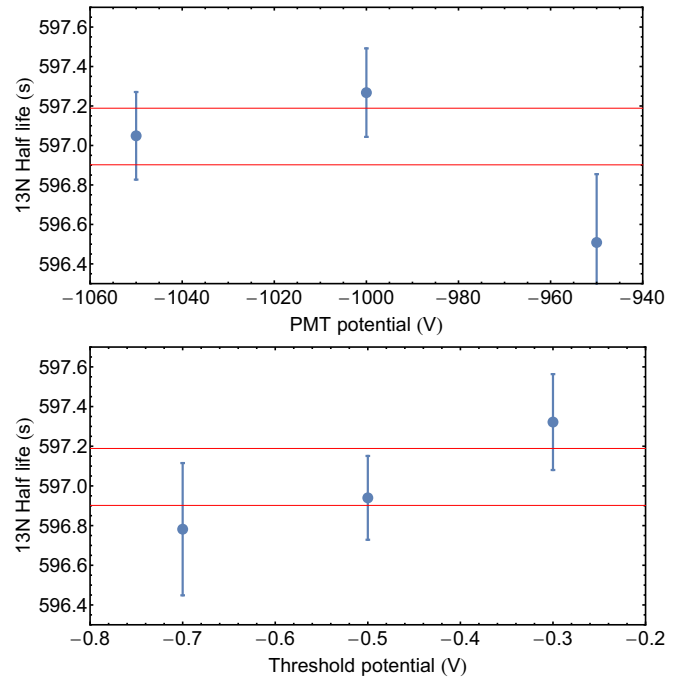


FIG. 9. Half-lives of ^{13}N when a *summed fit* is performed on all runs of identical PMT voltage and PMT discriminator threshold voltage. The one standard deviation uncertainty on the weighted average for each partition is given by solid lines.

is $1.30(28)$ and the Birge ratio for the discriminator threshold voltage grouping is $1.05(28)$.

Comparing these two Birge ratios shows that $1.30(28)$, the PMT grouping result, is the largest. This implies our uncertainty is underestimated. To account for this the uncertainty in the ^{13}N half-life from Sec. III B is multiplied by this larger Birge ratio giving a value of $597.05(19)$ s. The systematic uncertainties resulting from the dead time, choice of time binning, possible contamination, and the clock results were added in quadrature, giving a total systematic uncertainty of 55 ms. When added to the Birge-ratio inflated uncertainty from the fitting procedure, this yields an adopted ^{13}N half-life result of $597.05(19)$ s.

IV. ^{13}N HALF-LIFE

The new ^{13}N measurement of $597.05(19)$ s differs from the previous world value of $597.88(23)$ by 2.8σ while also being the most precise measurement to date. Using the new half-life from this work, a new world value was calculated by reevaluating the world data. The three measurements with the largest uncertainties [22–24] were removed from the evaluation due to their uncertainty being over ten times larger than the most precise measurement, as per the criteria used by Ref. [25] and the Particle Data Group [26].

Also, any measurements conducted before around 1969 are suspect because the importance of using a “maximum-likelihood” method of analysis, which is subject to less bias than conventional least-squares fitting, did not begin to be adopted more widely until 1969 [27]. Two measurements

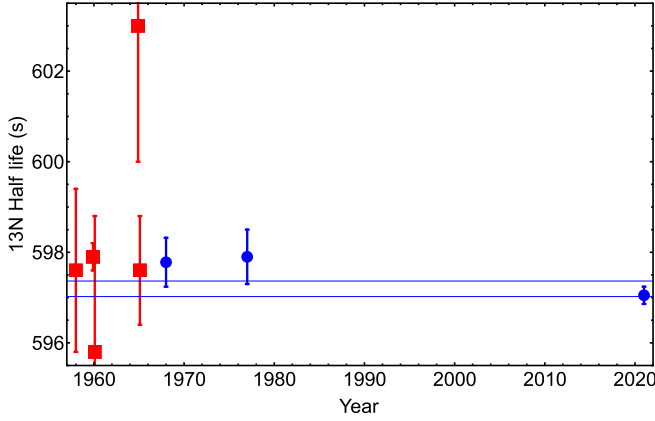


FIG. 10. ^{13}N half-lives [22–24,28–31] considered in the evaluation of the new world value. The square points were removed from our evaluation. The scaled uncertainty on the overall ^{13}N half-life of 597.19(22) s is represented by the two blue lines.

were found to explicitly cite the use of conventional least-squares fitting [28,29] and were removed from the world average. The half-life value used [30,31] to find the new world value are shown by the blue circles in Fig. 10, while the rejected measurements [22–24,28,29] are indicated by red squares. A weighted average yields a half-life of 597.19(17) s. This new world average is shown by the blue band in Fig. 10. The Birge ratio for this average is 1.25, implying that the uncertainty for several measurements in this data set are underestimated, so the uncertainty in the weighted average above is inflated by the Birge ratio giving a new world half-live value for ^{13}N of 597.19(22) s.

V. DISCUSSION

The ^{13}N half-life is one of three experimental quantities needed to calculate the ft value for the isospin $T = 1/2$ mixed transition, the others being the Q_{EC} value and the branching ratio. Using $Q_{EC} = 2220.47(27)$ keV from Ref. [32] and the parametrization from Ref. [33], a value of $f_v = 7.7143(72)$ was calculated. Then using the electron-capture fraction $P_{EC} = 0.196$, the branching ratio of 100%, and the theoretical corrections $\delta_R = 1.635(6)\%$, and $\delta_C^V - \delta_{NS}^V = 0.33(3)\%$ [34], the $\mathcal{F}t^{\text{mirror}}$ value was calculated. The $\mathcal{F}t^{\text{mirror}}$ values were calculated using both the half-lives from Ref. [34] and the new world value. The half-life from this work changes the $\mathcal{F}t^{\text{mirror}}$ value by 5.1 s while being slightly more precise. Using this $\mathcal{F}t^{\text{mirror}}$ value, we can extract a SM-predicted value for the mixing ratio ρ using [34]

$$\mathcal{F}t^{\text{mirror}} = \frac{2\mathcal{F}t^{0^+ \rightarrow 0^+}}{1 + \frac{f_A}{f_v}\rho^2}, \quad (4)$$

where $\mathcal{F}t^{0^+ \rightarrow 0^+} = 3072.24(185)$ s [3] is the average value of the 15 most precisely known pure Fermi $0^+ \rightarrow 0^+$ superallowed transitions and f_A is the axial-vector part of the statistical rate function. f_A was evaluated using the parametrization given in Ref. [33] and found to be 7.7488(72). Using this new SM-predicted value for ρ , the measurable

TABLE III. Values for various parameters of relevance for determining V_{ud} from the ^{13}N mirror transition. It is important to note that the given value ρ and the associated correlation parameters are predictions assuming the validity of the standard model.

Parameter	This work	With previous $t_{1/2}$
$t_{1/2}$	597.19(22) s	597.88(23) s
$f_v t$	4616.3(45) s	4621.3(47) s
$\mathcal{F}t^{\text{mirror}}$	4676.3(48) s	4681.4(49) s
ρ	0.5591(14)	0.5578(14)
a_{SM}	0.6825(12)	0.6836(13)
A_{SM}	-0.33308(4)	-0.33304(4)
B_{SM}	-0.6506(13)	-0.6495(13)

parameters a_{SM} , A_{SM} , and B_{SM} , all of which are summarized in Table III, were calculated assuming that the ^{13}N mirror transition obeys the standard model (SM).

VI. AB INITIO CALCULATION

In principle, sufficiently precise *ab initio* nuclear calculations could provide nonphenomenological estimates for the isospin symmetry-breaking corrections required to extract an accurate value of the V_{ud} element of the CKM matrix and test the SM. The calculated matrix elements reflect not only the many-body structure of the nucleus, which is of interest in its own right [35], but also the effects of meson-exchange currents (MECs) [36,37] or higher-order chiral corrections [38–41] to the weak-interaction decay operator. *Ab initio* calculations of the Gamow-Teller matrix elements in light nuclei have been carried out by quantum Monte Carlo methods [42] for $A \lesssim 10$ [36,40], or using the no-core configuration interaction (NCCI), or no-core shell model (NCSM), approach [43] for nuclei throughout the p shell [44–47]. The accuracy of such calculations is limited not only by the inputs to the calculation, i.e., the internucleon interaction and current operators, but also by the finite accuracy of the many-body calculation itself.

As a starting point for further understanding both of structural effects and of corrections to the weak-interaction decay operator in *ab initio* predictions for the $^{13}\text{N} \rightarrow ^{13}\text{C}$ decay, we carry out a baseline NCCI calculation for the Gamow-Teller matrix element. We use the Daejeon16 internucleon interaction [48], which is comparatively “soft,” thus facilitating convergence. This interaction, which is derived from the two-body part of the Entem-Machleidt N^3LO chiral effective-field theory (χEFT) interaction [49], but then softened via a similarity renormalization group (SRG) transformation [50] and adjusted via a phase-shift equivalent transformation to better describe nuclei with $A \leq 16$, provides a reasonable description of observables in p -shell nuclei [51]. We perform independent diagonalizations for the ^{13}N and ^{13}C ground-state wave functions (isospin symmetry is weakly broken by the Coulomb interaction), using the code MFDN [52,53] and then compute the Gamow-Teller matrix element between these wave functions by using the impulse approximation (i.e., $\frac{1}{2}\sigma\tau$) Gamow-Teller operator.

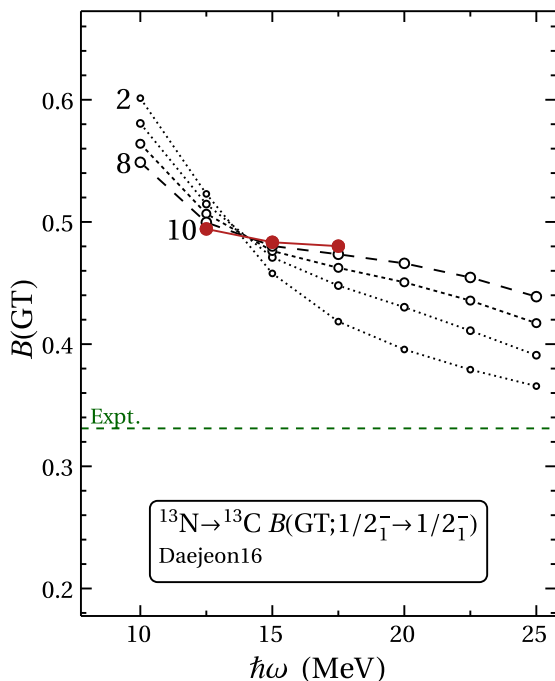


FIG. 11. NCCI calculated $B(\text{GT})$ value, as a function of basis oscillator parameter ($\hbar\omega$), in successively larger truncated spaces ($N_{\text{max}} = 2$ to 10, dotted to solid lines), for the Daejeon16 internucleon interaction.

The resulting calculated Gamow-Teller reduced transition probabilities, or $B(\text{GT})$ strengths, are shown in Fig. 11. Here $B(\text{GT})$ is related to the reduced matrix element of the Gamow-Teller operator $\frac{1}{2}\sigma\tau_{-}$ by $B(\text{GT}) = g_A^2 |\langle \psi_f | \frac{1}{2}\sigma\tau_{-} | \psi_i \rangle|^2 / (2J_i + 1)$ [54], where we have taken $g_A = 1.2754$ for the axial coupling strength [55].

For NCCI calculations, the accuracy is limited by the need to truncate the notionally infinite harmonic-oscillator Slater determinant basis used to describe the nuclear many-body wave functions. For calculations in a finite basis, the results for observables retain some dependence on the basis truncation parameters, namely, the maximum number N_{max} of oscillator excitations and the length scale or $\hbar\omega$ parameter of the underlying oscillator orbitals. As N_{max} increases, the calculated values approach those for the full, untruncated many-body problem, but the degree of convergence varies depending upon the observable, interaction, and states involved [56,57]. In Fig. 11, the flattening or “shouldering” of the curves with increasing N_{max} and the compression of successive curves against each other signal increasing N_{max} and $\hbar\omega$ independence, and thus an approach to convergence.

The value for $B(\text{GT})$ obtained from these calculations, with the Daejeon16 interaction in the impulse approximation, is thus seen to be ≈ 0.48 , where the remaining basis dependence suggests an uncertainty of approximately ± 0.05 . For comparison, the value for $B(\text{GT})$ extracted from the experimental $f_{\nu}t$ by assuming the SM and using the relation [1]

$$f_{\nu}t = \frac{2\pi\hbar^7 \ln 2}{m_e^5 c^4} \frac{1}{|G_F V_{ud}|^2 [B(\text{F}) + B(\text{GT})]} = \frac{2\mathcal{F}t^{0^+ \rightarrow 0^+}}{B(\text{F}) + B(\text{GT})}, \quad (5)$$

taking $B(\text{F}) = 1$, is $B(\text{GT}) \approx 0.33$. The deviation of the present predictions from the experimental value is of the order expected from higher-order chiral corrections in calculations for neighboring nuclei [40,47].

VII. CONCLUSION

A new precision half-life measurement of ^{13}N was performed at the NSL of UND using a ^{13}N RIB from the *TwinSol* facility. The new half-life of 597.05(22) s has a similar precision as the previous world average while differing by about 2.8σ , indicating the need for more independent half-life measurements. The $f_{\nu}t$ -value uncertainty is still dominated by the Q_{EC} value.

We also present the first NCCI calculation results using the Daejeon16 interaction for the $B(\text{GT})$ value of ^{13}N . The substantially higher value compared with experiment indicates that higher-order chiral corrections will likely need to be included in a future calculation of the isospin-symmetry-breaking correction.

Finally, in order to extract a value for V_{ud} or test for the presence of scalar currents, an experimental measurement of the mixing ratio ρ is required. To measure ρ for ^{13}N and other nuclei, the superallowed transition beta neutrino decay ion trap (St. Benedict) is currently under construction at the UND NSL [58–61].

ACKNOWLEDGMENTS

This work was supported in part by the National Science Foundation (NSF) Grants No. PHY-1713857, No. PHY-2011890, No. PHY-1401343, and No. PHY-1401242, and by the U.S. Department of Energy, Office of Science, under Award No. DE-FG02-95ER-40934. This research used computational resources of the National Energy Research Scientific Computing Center (NERSC), a U.S. Department of Energy, Office of Science, user facility supported under Contract No. DE-AC02-05CH11231.

- [1] M. González-Alonso, O. Naviliat-Cuncic, and N. Severijns, *Prog. Part. Nucl. Phys.* **104**, 165 (2019).
 [2] A. Falkowski, M. González-Alonso, and O. Naviliat-Cuncic, *J. High Energy Phys.* **04** (2021) 126.
 [3] J. C. Hardy and I. S. Towner, *Phys. Rev. C* **102**, 045501 (2020).

- [4] K. Gulyuz, G. Bollen, M. Brodeur, R. A. Bryce, K. Cooper, M. Eibach, C. Izzo, E. Kwan, K. Manukyan, D. J. Morrissey, O. Naviliat-Cuncic, M. Redshaw, R. Ringle, R. Sandler, S. Schwarz, C. S. Sumithrarachchi, A. A. Valverde, and A. C. C. Villari, *Phys. Rev. Lett.* **116**, 012501 (2016).

- [5] A. A. Valverde, M. Brodeur, T. Ahn, J. Allen, D. W. Bardayan, F. D. Becchetti, D. Blankstein, G. Brown, D. P. Burdette, B. Frentz, G. Gilardy, M. R. Hall, S. King, J. J. Kolata, J. Long, K. T. Macon, A. Nelson, P. D. O'Malley, M. Skulski, S. Y. Strauss *et al.*, *Phys. Rev. C* **97**, 035503 (2018).
- [6] O. Naviliat-Cuncic and N. Severijns, *Phys. Rev. Lett.* **102**, 142302 (2009).
- [7] M. S. Martin, S. R. Stroberg, J. D. Holt, and K. G. Leach, *Phys. Rev. C* **104**, 014324 (2021).
- [8] F. Becchetti, M. Lee, T. O'Donnell, D. Roberts, J. Kolata, L. Lamm, G. Rogachev, V. Guimarães, P. DeYoung, and S. Vincent, *Nucl. Instrum. Methods Phys. Res. Sect. A* **505**, 377 (2003).
- [9] T. Ahn *et al.*, *Nucl. Instrum. Methods Phys. Res. Sect. B* **376**, 321 (2016).
- [10] M. Brodeur, C. Nicoloff, T. Ahn, J. Allen, D. W. Bardayan, F. D. Becchetti, Y. K. Gupta, M. R. Hall, O. Hall, J. Hu, J. M. Kelly, J. J. Kolata, J. Long, P. O'Malley, and B. E. Schultz, *Phys. Rev. C* **93**, 025503 (2016).
- [11] J. Long, M. Brodeur, M. Baines, D. W. Bardayan, F. D. Becchetti, D. Blankstein, C. Boomershine, D. P. Burdette, A. M. Clark, B. Frentz, S. L. Henderson, J. M. Kelly, J. J. Kolata, B. Liu, K. T. Macon, P. D. O'Malley, A. Pardo, C. Seymour, S. Y. Strauss, and B. Vande Kolk, *Phys. Rev. C* **101**, 015501 (2020).
- [12] D. P. Burdette, M. Brodeur, D. W. Bardayan, F. D. Becchetti, D. Blankstein, C. Boomershine, L. Caves, S. L. Henderson, J. J. Kolata, B. Liu, J. Long, P. D. O'Malley, and S. Y. Strauss, *Phys. Rev. C* **101**, 055504 (2020).
- [13] A. Baerg, *Int. J. Appl. Radiat. Isot.* **24**, 401 (1973).
- [14] V. Koslowsky, E. Hagberg, J. Hardy, G. Savard, H. Schmeing, K. Sharma, and X. Sun, *Nucl. Instrum. Methods Phys. Res. Sect. A* **401**, 289 (1997).
- [15] J. Long, T. Ahn, J. Allen, D. W. Bardayan, F. D. Becchetti, D. Blankstein, M. Brodeur, D. Burdette, B. Frentz, M. R. Hall, J. M. Kelly, J. J. Kolata, P. D. O'Malley, B. E. Schultz, S. Y. Strauss, and A. A. Valverde, *Phys. Rev. C* **96**, 015502 (2017).
- [16] D. P. Burdette, M. Brodeur, T. Ahn, J. Allen, D. W. Bardayan, F. D. Becchetti, D. Blankstein, G. Brown, B. Frentz, M. R. Hall, S. King, J. J. Kolata, J. Long, K. T. Macon, A. Nelson, P. D. O'Malley, C. Seymour, M. Skulski, S. Y. Strauss, and A. A. Valverde, *Phys. Rev. C* **99**, 015501 (2019).
- [17] A. P. Baerg, *Metrologia* **1**, 131 (1965).
- [18] J. W. Fowler, *J. Low Temp. Phys.* **176**, 414 (2014).
- [19] S. Baker and R. D. Cousins, *Nucl. Instrum. Methods Phys. Res.* **221**, 437 (1984).
- [20] G. F. Grinyer, C. E. Svensson, C. Andreoiu, A. N. Andreyev, R. A. E. Austin, G. C. Ball, R. S. Chakrawarthy, P. Finlay, P. E. Garrett, G. Hackman, J. C. Hardy, B. Hyland, V. E. Iacob, K. A. Koopmans, W. D. Kulp, J. R. Leslie, J. A. Macdonald, A. C. Morton, W. E. Ormand, C. J. Osborne *et al.*, *Phys. Rev. C* **71**, 044309 (2005).
- [21] R. T. Birge, *Phys. Rev.* **40**, 207 (1932).
- [22] S. E. Arnell, J. Dubois, and O. Almén, *Nucl. Phys.* **6**, 196 (1958).
- [23] J. D. King, R. N. H. Haslam, and R. W. Parsons, *Can. J. Phys.* **38**, 231 (1960).
- [24] M. Bormann, E. Fretwurst, P. Schehka, G. Wrege, H. Büttner, A. Lindner, and H. Meldner, *Nucl. Phys.* **63**, 438 (1965).
- [25] J. C. Hardy and I. S. Towner, *Phys. Rev. C* **71**, 055501 (2005).
- [26] J. Beringer *et al.* (Particle Data Group), *Phys. Rev. D* **86**, 010001 (2012).
- [27] J. C. Hardy and I. S. Towner, *Phys. Rev. C* **91**, 025501 (2015).
- [28] J. Jänecke, *Z. Naturforsch. A: Phys. Sci.* **15**, 593 (1960).
- [29] T. G. Ebrey and P. R. Gray, *Nucl. Phys.* **61**, 479 (1965).
- [30] A. Ritchie, *Nucl. Instrum. Methods* **64**, 181 (1968).
- [31] G. Azuelos, J. E. Kitching, and K. Ramavataram, *Phys. Rev. C* **15**, 1847 (1977).
- [32] M. Wang, W. Huang, F. Kondev, G. Audi, and S. Naimi, *Chin. Phys. C* **45**, 030003 (2021).
- [33] I. S. Towner and J. C. Hardy, *Phys. Rev. C* **91**, 015501 (2015).
- [34] N. Severijns, M. Tandecki, T. Phalet, and I. S. Towner, *Phys. Rev. C* **78**, 055501 (2008).
- [35] D. J. Millener and D. Kurath, *Nucl. Phys. A* **255**, 315 (1975).
- [36] R. Schiavilla and R. B. Wiringa, *Phys. Rev. C* **65**, 054302 (2002).
- [37] J. T. Suhonen, *Front. Phys.* **5**, 55 (2017).
- [38] A. Baroni, L. Girlanda, S. Pastore, R. Schiavilla, and M. Viviani, *Phys. Rev. C* **93**, 015501 (2016).
- [39] A. Baroni, R. Schiavilla, L. E. Marcucci, L. Girlanda, A. Kievsky, A. Lovato, S. Pastore, M. Piarulli, S. C. Pieper, M. Viviani, and R. B. Wiringa, *Phys. Rev. C* **98**, 044003 (2018).
- [40] S. Pastore, A. Baroni, J. Carlson, S. Gandolfi, S. C. Pieper, R. Schiavilla, and R. B. Wiringa, *Phys. Rev. C* **97**, 022501(R) (2018).
- [41] H. Krebs, E. Epelbaum, and U.-G. Meißner, *Ann. Phys. (NY)* **378**, 317 (2017).
- [42] J. Carlson, S. Gandolfi, F. Pederiva, S. C. Pieper, R. Schiavilla, K. E. Schmidt, and R. B. Wiringa, *Rev. Mod. Phys.* **87**, 1067 (2015).
- [43] B. R. Barrett, P. Navrátil, and J. P. Vary, *Prog. Part. Nucl. Phys.* **69**, 131 (2013).
- [44] E. Caurier, P. Navrátil, W. E. Ormand, and J. P. Vary, *Phys. Rev. C* **66**, 024314 (2002).
- [45] P. Maris, J. P. Vary, P. Navrátil, W. E. Ormand, H. Nam, and D. J. Dean, *Phys. Rev. Lett.* **106**, 202502 (2011).
- [46] C. Cockrell, J. P. Vary, and P. Maris, *Phys. Rev. C* **86**, 034325 (2012).
- [47] P. Gysbers, G. Hagen, J. D. Holt, G. R. Jansen, T. D. Morris, P. Navrátil, T. Papenbrock, S. Quaglioni, A. Schwenk, S. R. Stroberg, and K. A. Wendt, *Nat. Phys.* **15**, 428 (2019).
- [48] A. M. Shirokov, I. J. Shin, Y. Kim, M. Sosonkina, P. Maris, and J. P. Vary, *Phys. Lett. B* **761**, 87 (2016).
- [49] D. R. Entem and R. Machleidt, *Phys. Rev. C* **68**, 041001(R) (2003).
- [50] S. K. Bogner, R. J. Furnstahl, and R. J. Perry, *Phys. Rev. C* **75**, 061001(R) (2007).
- [51] P. Maris, I. J. Shin, and J. P. Vary, *Proceedings of the International Conference Nuclear Theory in the Supercomputing Era 2018*, edited by A. M. Shirokov and A. I. Mazur (Pacific National University, Khabarovsk, 2019), p. 168.
- [52] H. M. Aktulga, C. Yang, E. G. Ng, P. Maris, and J. P. Vary, *Concurr. Comput.* **26**, 2631 (2014).
- [53] M. Shao, H. M. Aktulga, C. Yang, E. G. Ng, P. Maris, and J. P. Vary, *Comput. Phys. Commun.* **222**, 1 (2018).
- [54] J. Suhonen, *From Nucleons to Nucleus* (Springer-Verlag, Berlin, 2007).
- [55] P. A. Zyla *et al.* (Particle Data Group), *Prog. Theor. Exp. Phys.* **2020**, 083C01 (2020).
- [56] S. K. Bogner, R. J. Furnstahl, P. Maris, R. J. Perry, A. Schwenk, and J. Vary, *Nucl. Phys. A* **801**, 21 (2008).

- [57] P. Maris and J. P. Vary, [Int. J. Mod. Phys. E](#) **22**, 1330016 (2013).
- [58] M. Brodeur, J. Kelly, J. Long, C. Nicoloff, and B. Schultz, [Nucl. Instrum. Methods Phys. Res. Sect. B](#) **376**, 281 (2016).
- [59] D. Burdette, M. Brodeur, P. O'Malley, and A. Valverde, [Hyperfine Interact.](#) **240**, 70 (2019).
- [60] A. A. Valverde, M. Brodeur, D. P. Burdette, J. A. Clark, J. W. Klimes, D. Lascar, P. D. O'Malley, R. Ringle, G. Savard, and V. Varentsov, [Hyperfine Interact.](#) **240**, 38 (2019).
- [61] P. O'Malley, M. Brodeur, D. Burdette, J. Klimes, A. Valverde, J. Clark, G. Savard, R. Ringle, and V. Varentsov, [Nucl. Instrum. Methods Phys. Res. Sect. B](#) **463**, 488 (2020).